INTERNATIONAL JOURNAL FOR NUMERICAL METHODS IN FLUIDS
*Int. J. Numer. Meth. Fluids* 2004; **45**:921–944 (DOI: 10.1002/fld.715)

# Numerical analysis of moving interfaces using a level set method coupled with adaptive mesh refinement

Haruhiko Kohno*,† and Takahiko Tanahashi

*Keio University, 3-14-1, Hiyoshi, Kohoku-ku, Yokohama 223-8522, Japan*

SUMMARY

A novel numerical scheme is developed by coupling the level set method with the adaptive mesh refinement in order to analyse moving interfaces economically and accurately. The finite element method (FEM) is used to discretize the governing equations with the generalized simplified marker and cell (GSMAC) scheme, and the cubic interpolated pseudo-particle (CIP) method is applied to the reinitialization of the level set function. The present adaptive mesh refinement is implemented in the quadrangular grid systems and easily embedded in the FEM-based algorithm. For the judgement on renewal of mesh, the level set function is adopted as an indicator, and the threshold is set at the boundary of the smoothing band. With this criterion, the variation of physical properties and the jump quantity on the free surface can be calculated accurately enough, while the computation cost is largely reduced as a whole. In order to prove the validity of the present scheme, two-dimensional numerical simulation is carried out in collapse of a water column, oscillation and movement of a drop under zero gravity. As a result, its effectiveness and usefulness are clearly shown qualitatively and quantitatively. Among them, the movement of a drop due to the Marangoni effect is first simulated efficiently with the present scheme.


KEY WORDS: level set method; adaptive mesh refinement; moving free surface; surface tension; Marangoni effect; GSMAC

## 1. INTRODUCTION

The movement of a free surface can be seen in various situations in our daily life: e.g. sloshing in a water tank, rippling in a pond, merging and breaking of bubbles. In the engineering fields, such moving interfaces are often controlled for the purpose of stabilization in production process and maintenance of quality. Although the evolution of a free surface is largely affected by gravity on the ground, it is governed by surface tension in space due to the microgravity condition. This should be kept in mind in the material experiments, e.g. floating zone crystal growth [1] and levitation melting [2], which will be vigorously performed in the international

*Correspondence to: H. Kohno, Keio University, 3-14-1, Hiyoshi, Kohoku-ku, Yokohama 223-8522, Japan.
†E-mail: kohno@tana.mech.keio.ac.jp

Contract/grant sponsor: Ministry of Education, Culture, Sports, Science and Technology of Japan

Published online 4 May 2004
Copyright © 2004 John Wiley & Sons, Ltd.
*Received 26 August 2003*
*Revised 26 January 2004*

space station in the near future. For the reasons mentioned above, there is much demand for the numerical schemes that handle a variety of moving interface problems.

In order to calculate the movement of a free surface, a number of methods have been proposed so far. They can be classified into two groups: the Eulerian methods and the Lagrangian methods [3]. In the former, the moving interface is implicitly captured by a scalar function with the grids covering the liquid region and the gas region fixed. Thus, the calculation is conducted stably no matter how complicated the interface evolves. Furthermore, the extension from 2 to 3 dimensions can be achieved easily. However, since the free surface is positioned between the nodal points, the accuracy is so dependant on grid size that fine grids are necessary to obtain good results; it requires time-consuming computation. In this category, the marker and cell (MAC) method [4], the volume of fluid (VOF) method [5–8] and the level set method [9–15] have been widely accepted. On the other hand, the profile of the free surface is determined by the positions of the exterior grid nodes in the latter. These grid nodes correspond to the fluid particles on the interface, so the moving surface is explicitly tracked by them according to the advection equation. Grids are allocated to only the liquid region, so that the fluid flow in the gas is not considered. Compared to the former methods, the moving free surface is computed more precisely and sharply when the same grid resolution is provided. Furthermore, the boundary conditions on the interface can be applied in a straightforward way. When the grids are extremely distorted in accordance with the deformation of a free surface, the rezoning process, whose algorithm is referred as the arbitrary Lagrangian–Eulerian (ALE) method [16–18], is necessary to avoid the failure due to inaccuracy in the solution of the flow field. However, some problems, such as merging, breaking and self-intersecting, cannot be solved even by them. In addition, the rezoning algorithm becomes very complicated in case a free surface surrounds the analytical object and moves three dimensionally.

In the present study, a numerical scheme that realizes high-speed calculation, stability and accuracy in the computation of two-dimensional free-surface flows is developed by coupling the level set method with the adaptive mesh refinement in which grid fining and coarsening are performed together. Although some similar approaches have been reported so far [7, 14, 15], their applications are restricted within narrow limits, and only a few studies investigate the relation between accuracy and computation time quantitatively. Moreover, the movement of a drop due to the Marangoni effect [19–24] has not been analysed with the relevant methods yet. The governing equations are discretized by the finite element method (FEM), in which the velocity field is solved by the generalized simplified marker and cell (GSMAC) scheme [25–28] and the cubic interpolated pseudo-particle (CIP) method [29] is applied to the reinitialization of the level set function. The outline of the paper is as follows: first the governing equations and their discretization are described with a review of the level set method. Next, all the particulars of the adaptive mesh refinement based on two-dimensional quadrangular grids are given, in which the splitting criterion is mentioned. Finally, the effectiveness and usefulness of the present scheme are evaluated qualitatively and quantitatively in the following three examples: collapse of a water column, oscillation and movement of a drop under zero gravity.

## 2. GOVERNING EQUATIONS

The governing equations in the flow field are the equation of continuity and the incompressible Navier–Stokes equation, which are written in the following dimensionless forms:

$$\nabla \cdot \mathbf{v} = 0 \tag{1}$$

 

isothermal case

$$\rho\left(\frac{\partial \mathbf{v}}{\partial t}+\mathbf{v}\cdot\nabla\mathbf{v}\right)=-\nabla p+\frac{\mu}{Re}\nabla^2\mathbf{v}-\frac{1}{Bo}(\nabla\cdot\mathbf{n})\mathbf{n}\delta_\varepsilon+\rho\mathbf{e} \tag{2}$$

non-isothermal case

$$\rho\left(\frac{\partial \mathbf{v}}{\partial t}+\mathbf{v}\cdot\nabla\mathbf{v}\right)=-\nabla p+\frac{\mu}{Re}\nabla^2\mathbf{v}+\left\{\frac{Ma}{Re\,Pe}\nabla_{//}T-\frac{1}{We}(\nabla\cdot\mathbf{n})\mathbf{n}\right\}\delta_\varepsilon \tag{3}$$

where $\mathbf{v}, \rho, t, p, \mu, \mathbf{n}, \delta_\varepsilon, \mathbf{e}, \nabla_{//}$ and $T$ are the velocity, density, time, pressure, coefficient of viscosity, unit normal vector pointing to the gas phase, approximate Delta function, unit vector whose direction corresponds to that of gravity, surface nabla operator and temperature, respectively. The dimensionless parameters $Re \equiv UL/\nu_0$, $Bo \equiv \rho_0 g L^2/\sigma_s$, $Ma \equiv \sigma_T L \Delta T_0/\mu_0\alpha_0$, $Pe \equiv UL/\alpha_0$ and $We \equiv \rho_0 U^2 L/\sigma_s$ are the Reynolds number, Bond number, Marangoni number, Peclet number and Weber number, respectively; $U$ is the representative velocity, $L$ the representative length, $\nu$ the kinematic viscosity, $g$ the gravitational acceleration, $\sigma_s$ the surface tension, $\sigma_T$ the thermal coefficient of surface tension, $\alpha$ the thermal diffusivity and the representative values of the physical properties are shown with the subscript 0. In the present study, the Navier–Stokes equation (2) is used for the analysis in which the temperature field is not considered under the normal gravity condition, whereas Equation (3) includes the effect from the temperature field under zero gravity. The third terms in Equations (2), (3) and the fourth term in Equation (3) on the right-hand sides are derived from the jump quantity of the stress vector $[\mathbf{t}^{(n)}], [\mathbf{t}^{(n)}] = \nabla_{//}\sigma_s - \sigma_s(\nabla\cdot\mathbf{n})\mathbf{n}$ [30]. Since the surface tension depends on temperature, the shearing force is induced by the gradient of surface tension on the free surface, which is called Marangoni effect and corresponds to the third term in Equation (3). In addition, the restoring force produces movement of the interface to minimize the surface area, which corresponds to the third term in Equation (2) and the fourth term in Equation (3). The temperature field is governed by the energy equation, which is written as follows:

$$\frac{\partial T}{\partial t}+\mathbf{v}\cdot\nabla T=\frac{\alpha}{Pe}\nabla^2 T \tag{4}$$

The discontinuous change of the physical properties on the free surface is smoothed by the approximate Heaviside function $H_\varepsilon$ as follows:

$$\begin{cases} H_\varepsilon(F)=0 & \text{if } F<-\varepsilon \\ H_\varepsilon(F)=\dfrac{1}{2}\left\{1+\dfrac{F}{\varepsilon}+\dfrac{1}{\pi}\sin\left(\dfrac{\pi F}{\varepsilon}\right)\right\} & \text{if } |F|\leqslant\varepsilon \\ H_\varepsilon(F)=1 & \text{if } F>\varepsilon \end{cases} \tag{5}$$

where $F$ is the level set function, and $\varepsilon$ the smoothing bandwidth. The level set function is defined as a vertical distance from the interface to each node with signs in order to distinguish one phase from the other; the liquid phase lies in $F<0$, and the gas phase does in $F>0$ in the present study. The approximate Delta function is obtained by differentiating the approximate Heaviside function and combined with the surface forces as shown in Equations (2) and (3), so that the jump quantity on the free surface can be calculated as a body force [30]. The physical properties are defined in one generic equation, $q = H_\varepsilon q_G/q_L + (1-H_\varepsilon)$ where $q$ being

 

the density, the coefficient of viscosity or the thermal diffusivity; the subscript G denotes the gas phase, and L does the liquid phase.

The position of a free surface is captured implicitly by the level set function defined at each node. The interface, i.e. $F = 0$, moves according to the following kinematic condition:

$$\frac{\partial F}{\partial t} + \mathbf{v}\cdot\nabla F = 0 \tag{6}$$

However, the nature of the level set function as a distance function gets lost except the position of the interface since Equation (6) is calculated in the whole domain, where two fluids flow in every direction. Therefore, reinitialization is subsequently conducted to recover the nature of the function with the following equation [10]:

$$\begin{aligned} \frac{\partial F}{\partial \tau} + \mathbf{w}\cdot\nabla F &= S(F_0) \\ \mathbf{w} &= S(F_0)\frac{\nabla F}{|\nabla F|} \\ S(F_0) &= \frac{F_0}{\sqrt{F_0^2 + \varepsilon^2}} \end{aligned} \tag{7}$$

where $\tau$ is the quasi-time, and $F_0$ is the level set function obtained from Equation (6). Since the interface is positioned implicitly in the level set method, the total volume of a fluid may fluctuate during the reinitialization process. In order to preserve the initial volume, the following equation is solved at all nodes:

$$F = F_{\mathrm{r}} + \frac{V(t) - V_{\mathrm{init}}}{S(t)} \tag{8}$$

where $V(t)$ and $S(t)$ are, respectively, the calculated volume and area, which are regarded as area and line in 2 dimension, $F_{\mathrm{r}}$ the level set function obtained after the reinitialization and $V_{\mathrm{init}}$ is the initial volume. The second term on the right-hand side in Equation (8) equals to the length for modification on the calculated volume.

## 3. FINITE ELEMENT FORMULATION

The Navier–Stokes equation (3) is discretized by semi-implicit formulation, where the velocity and the pressure are, respectively, discretized explicitly and implicitly, whereas the energy equation (4) and the advection equation (6) for the moving interface are discretized by explicit formulation. According to the Galerkin method, Equations (3), (4) and (6) are rewritten in the element matrix forms as shown in Figure 1. The time marching algorithm is obtained by considering the equation of continuity, i.e. $\nabla\cdot\mathbf{v}^{n+1} = 0$ according to the GSMAC method. This is based on the idea of the highly simplified marker and cell (HSMAC) scheme [31], so that high-speed calculation is realized by introducing the simultaneous relaxation method. Here, $\tilde{\mathbf{v}}$ is the intermediate value of velocity, $\Delta t$ the increment of time, $\Omega^{\mathrm{e}}$ the area of an element, $\lambda^{-1}$ the inverse Laplace operator and $\phi_{\mathrm{p}}$ is the modified momentum potential defined

 

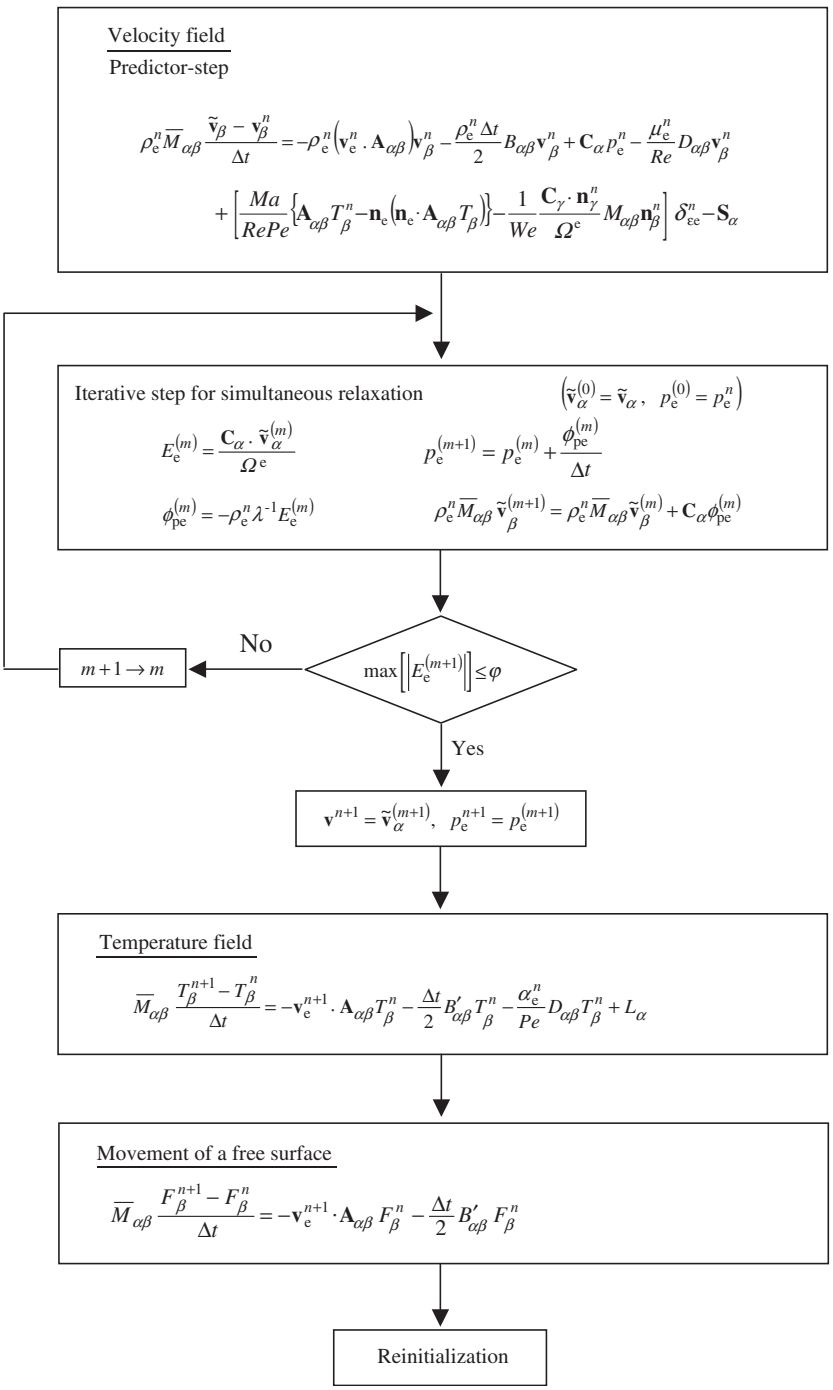


Figure 1. Flow chart of the present scheme.

 

$$\mathbf{A}_{\alpha\beta} = \int_{\Omega^e} N_\alpha \nabla N_\beta \, d\Omega$$

$$B_{\alpha\beta} = \int_{\Omega^e} \left(\mathbf{v}_e^n \cdot \nabla N_\alpha\right)\left(\mathbf{v}_e^n \cdot \nabla N_\beta\right) d\Omega$$

$$B'_{\alpha\beta} = \int_{\Omega^e} \left(\mathbf{v}_e^{n+1} \cdot \nabla N_\alpha\right)\left(\mathbf{v}_e^{n+1} \cdot \nabla N_\beta\right) d\Omega$$

$$\mathbf{C}_\alpha = \int_{\Omega^e} \nabla N_\alpha \, d\Omega$$

$$D_{\alpha\beta} = \int_{\Omega^e} \left(\nabla N_\alpha\right) \cdot \left(\nabla N_\beta\right) d\Omega$$

$$M_{\alpha\beta} = \int_{\Omega^e} N_\alpha N_\beta \, d\Omega$$

$$\mathbf{S}_\alpha = \int_{\Gamma_2^e} N_\alpha \left(p^n \mathbf{n}_\Gamma^n - \frac{\mu^n}{Re} \frac{\partial \mathbf{v}^n}{\partial n_\Gamma}\right)_e d\Gamma$$

$$L_\alpha = \int_{\Gamma_2^e} N_\alpha \left(\frac{\alpha^n}{Pe} \frac{T^n}{\partial n_\Gamma}\right)_e d\Gamma$$

Figure 2. The element coefficient matrices and boundary terms.

as $\phi_p = p^c \Delta t$; $p^c$ is the modified pressure, i.e. $p^c = p^{n+1} - p^n$. The subscripts $\alpha$ and $\beta$ denote the local node number, and the variables with the subscript e are constants on the elements. The superscripts $n$ and $m$ denote the $n$th time step and the iterative calculation level of the Poisson equation, respectively. The velocity components and the temperature are interpolated with bilinear interpolation functions $N_\alpha$, and the pressure is constant in each element. For the Poisson equation, the weighting function is equal to unity in order to utilize simultaneous relaxation based on the Newton–Raphson method. The element coefficient matrices and the boundary terms are calculated as shown in Figure 2. Here, $\Gamma$ denotes the interface, and $\bar{M}_{\alpha\beta}$ is the lamped mass matrix.

As mentioned in Section 2, the purpose of the reinitialization is to restore the distribution of the level set function. This is achieved by transmitting the interface configuration throughout the calculation domain with an upwind method. For that reason, CIP-FEM [32, 33] is applied to the solution of Equation (7). In the CIP method, the advection equation is solved according to the idea of the exact solution. Since the shape function including the value of the level set function and its derivatives are used for the interpolation with the accuracy of third order, the accurate results can be obtained even with relatively coarse grid systems. After discretizing

 

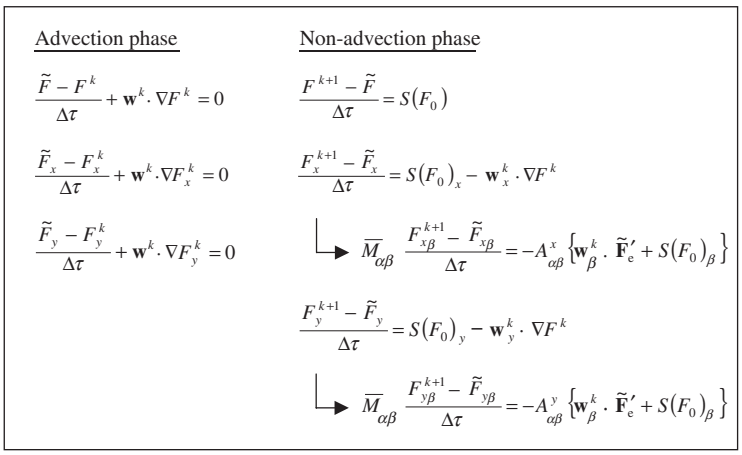


Figure 3. The advection and non-advection phases in the reinitialization.

Equation (7) and its differential explicitly, they are separated into two phases as shown in Figure 3. Here, $\tilde{F}$ is the intermediate value of the level set function, and $\Delta\tau$ is the increment of quasi-time; the subscripts $x$ and $y$ denote the differential in each direction, and the superscript $k$ denotes the iterative calculation level. First, the advection phase is solved by CIP-FEM. Then, the modified level set function and its derivatives are calculated in the non-advection phase. As shown, two equations in the non-advection phase are discretized by the Galerkin method, where the coefficient matrices $A_{\alpha\beta}^x$ and $A_{\alpha\beta}^y$ are, respectively, the $x$ and $y$ components of $\mathbf{A}_{\alpha\beta}$, and $\tilde{\mathbf{F}}'=(\tilde{F}_x,\tilde{F}_y)$.

In order to preserve the initial volume of a fluid, numerically fluctuated volume and area of the liquid phase are, respectively, calculated as follows:

$$V(t)=\int_\Omega\{1-H_\varepsilon(t)\}\,\mathrm{d}\Omega\cong\sum_{e=1}^{M}\{1-H_{\varepsilon e}(t)\}\Omega^e \tag{9}$$

$$S(t)=\int_\Omega\delta_\varepsilon(t)\,\mathrm{d}\Omega\cong\sum_{e=1}^{M}\delta_{\varepsilon e}(t)\Omega^e \tag{10}$$

where $M$ is the number of elements. Then, the level set function is finally determined by substituting Equations (9) and (10) into Equation (8).

## 4. INTRODUCTION OF THE ADAPTIVE MESH REFINEMENT

Large deformation problems, which often include merging or breaking of the analytical objects, can be solved stably by adopting the interface-capturing techniques, or Eulerian methods such as a level set method. However, more calculation grids are necessary for these techniques

 

to obtain the accurate results compared with the interface-tracking techniques, or Lagrangian methods, in which the grids are explicitly deformed in conjunction with the interface shape. This is caused by the fact that the interface position is secondarily determined in the former; if the number of grid nodes, which are regarded as observation points for the interface, are small in the level set method, the error due to lack of information becomes serious. For that reason, fine grids should be prepared in the calculation domain to obtain the desirable results in case the interface-capturing techniques are applied to the moving interface problem. However, the free surface configuration can be obtained accurately enough if only the calculation grids are provided finely in the vicinity of the interface. In addition, it is meaningless to conduct precise calculation in the area away from the free surface since the fluid motion around there hardly affects the behaviour of the interface, and the distribution of the level set function is corrected by reinitialization. Therefore, the application of the adaptive mesh refinement, which forms the distribution of calculation grids dynamically in connection with the interface position, would be effective in order to enhance the computational efficiency with the accuracy kept good. The following is the details of the adaptive mesh refinement developed in the present study.

### *4.1. Determination of the threshold*

The present adaptive mesh refinement consists of two main steps: grid fining and coarsening. In computation, the grids are divided finely in the area where some noticeable physical phenomena exist and high resolution is necessary to simulate them, while they are deleted and returned to the initial state in the other area where the accuracy in space is not so important. Here, the threshold of fining or coarsening should be determined carefully since the computational accuracy and efficiency are often sensitively affected by that. In practice, this technique especially takes effect when an object of interest is clearly distinguished from the others, e.g. unsteady shock wave in compressible fluid [34]. As a free surface also has the nature of discontinuity similar to the shock wave, the application of the adaptive mesh refinement should be effective.

In the present study, we aim at developing the adaptive mesh refinement in which the grids in the vicinity of the free surface are divided finely, whereas the grids are kept coarse in the area away from the interface. Even in such condition, the observation points for a free surface are provided enough, and the velocity vector on the interface can be calculated accurately, so that the interface moves smoothly and correctly at all time. In the process, the level set function is conveniently utilized for the judgement on renewal of mesh since the position of the free surface corresponds to the constant value of the function, i.e. $F = 0$. The threshold is set at the boundary of the smoothing band; the grids are divided on the condition of $|F| \leqslant \varepsilon$, while they are deleted on $|F| > \varepsilon$. The reason why we decide the criterion like this is that the variation of the physical properties and the jump quantity on the free surface, which should be calculated accurately, exist only within the smoothing band as mentioned in Section 2. Outside of the band, it is not necessary to calculate them since the physical properties are constant, and the jump quantity does not exist there.

### *4.2. Rules for grid fining and coarsening*

In the present adaptive mesh refinement, grid fining and coarsening are conducted together in the two-dimensional quadrangular grids, and the maximum division level can be set freely as

 

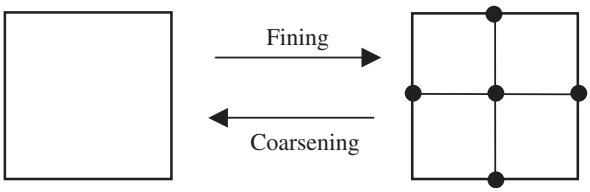


Figure 4. Procedures of the grid fining and coarsening.

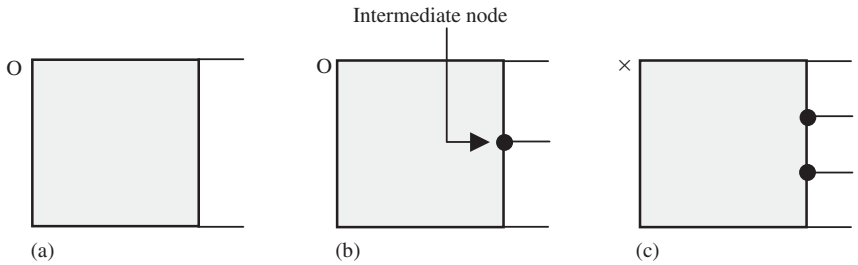


Figure 5. A rule for the number of next elements: (a) One element (b) two elements (c) three elements.

well as frequency of the mesh refinement. Rules for the grid division and deletion are given below.

As shown in Figure 4, a quadrangular grid is divided into four pieces when it satisfies the criterion for grid fining. Since the level set function is calculated at nodes, its average in an element is used for the judgement. After the fining procedure, five new nodes are added; one is positioned at the centre of a grid element, and the others are at the centre of each side. This state is called 'division level 1' if the initial grid is chosen as an object of grid fining. Similarly, the division level 2 is formed on the basis of the division level 1.

In the process of mesh refinement, grids with different size are mingled in the calculation domain. Here, a restriction is imposed on the number of adjacent elements; an element may border on eight elements, which corresponds to two elements in one side, at a maximum as shown in Figure 5. When the elements with different division levels adjoin, intermediate nodes, which are shared by three elements, are inevitably appeared as shown in Figure 5(b). However, since FEM is applied to the whole calculation, it is difficult to handle such nodes, especially in lumping the element values. Therefore, in order to introduce the adaptive mesh refinement without changing the algorithm for the flow field, the intermediate nodes should be excluded by making the connective grids as shown in Figure 6(a). In case a new intermediate node comes out as shown in Figure 6(b), additional connective grids are made in the adjacent element in order to eliminate the unfavourable character stated above.

In the grid coarsening, the connective grids and the child elements formed in the previous division process, which are, respectively, shown in Figures 6 and 4, are the objects of dele-

 

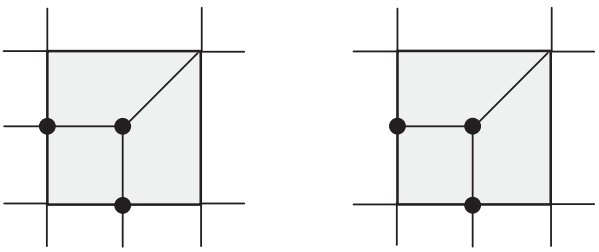


Figure 6. Two cases of the connective grids: (a) complete case (b) incomplete case.

tion under some conditions. The former are unconditionally deleted at the beginning of the algorithm, whereas the latter are done only in the case that the following four conditions are simultaneously satisfied:

- four child elements, which are named C1, C2, C3 and C4 in Figure 7, have the same division level and adjoin each other (see Figure 7(a)),
- the division levels of the elements adjacent to the child elements are not exceeding that of the child elements (see Figure 7(b)),
- the division levels of the elements positioned diagonally to the right or left of the child elements are not exceeding that of the child elements (see Figure 7(c)),
- the average of the four element values of the level set function satisfies the criterion for grid deletion, i.e. $|F| > \varepsilon$.

Therefore, the grid coarsening is carried out from the elements with the highest division level. The initial grids are not deleted in the present algorithm.

### *4.3. Interpolation of the physical quantities*

In order to continue the calculation of fluid flow with new mesh formed after the refinement, interpolated physical quantities are given to the new nodes or elements. In the present analysis, the velocity, temperature, level set function and its derivatives are defined at the nodes, whereas the pressure is done on the elements.

In the grid fining, the linear interpolation is adopted as an interpolation method for the physical quantities defined at the nodes as shown in Figure 8(a). The average of two values at the end nodes is given to a new node positioned at the centre of the side, and the average of four values at the apex nodes is done to a new node at the centre of the element. On the other hand, the value on a previous element is simply utilized for the constant value on a new element.

In the grid coarsening, the interpolation of the physical quantity defined on the elements is conducted by using the weighted average, in which the areas of the previous grids are considered as shown in Figure 8(b). The quantities defined at the nodes being deleted are eliminated from the grids.

 

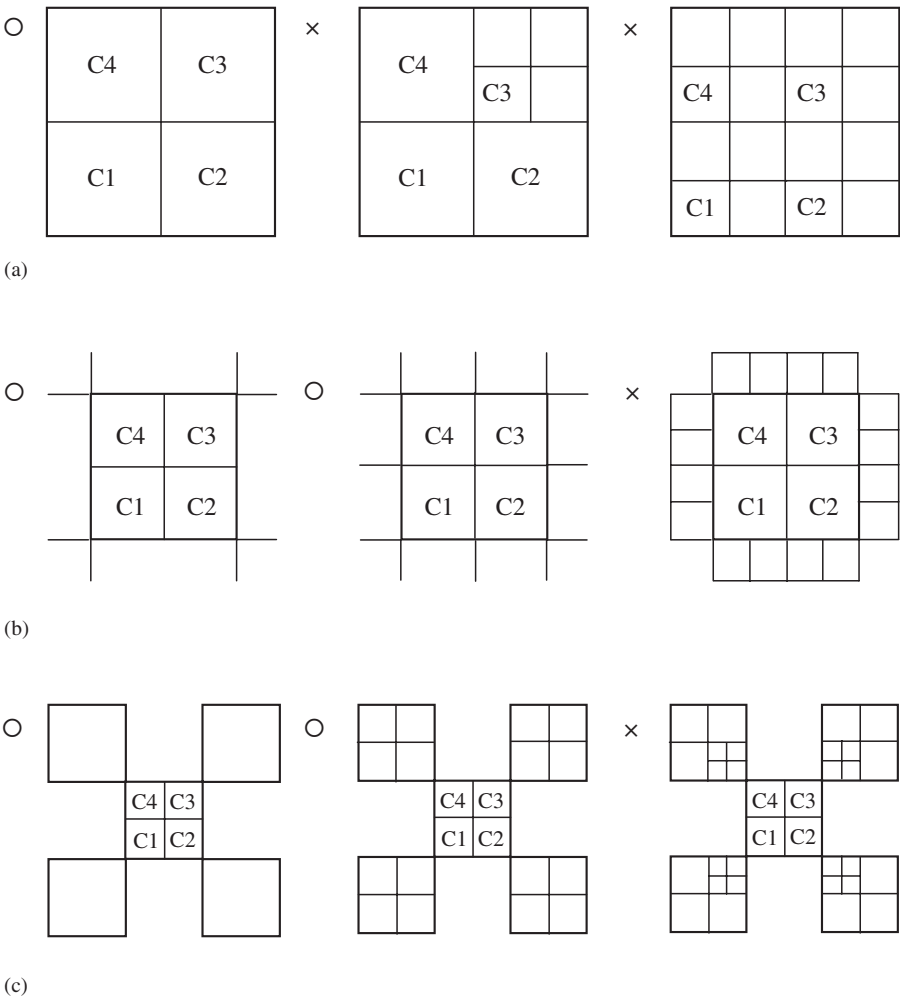


Figure 7. Conditions for the grid coarsening: (a) condition 1 (b) condition 2 (c) condition 3.

### *4.4. Algorithm*

All the steps in the adaptive mesh refinement are itemized in order as follows:

(1) deletion of the connective grids,
(2) rearrangement of the element and node numbers,
(3) deletion of the grids based on the criterion,
(4) rearrangement of the element and node numbers,
(5) division of the grids based on the criterion,
(6) formation of the connective grids.

 

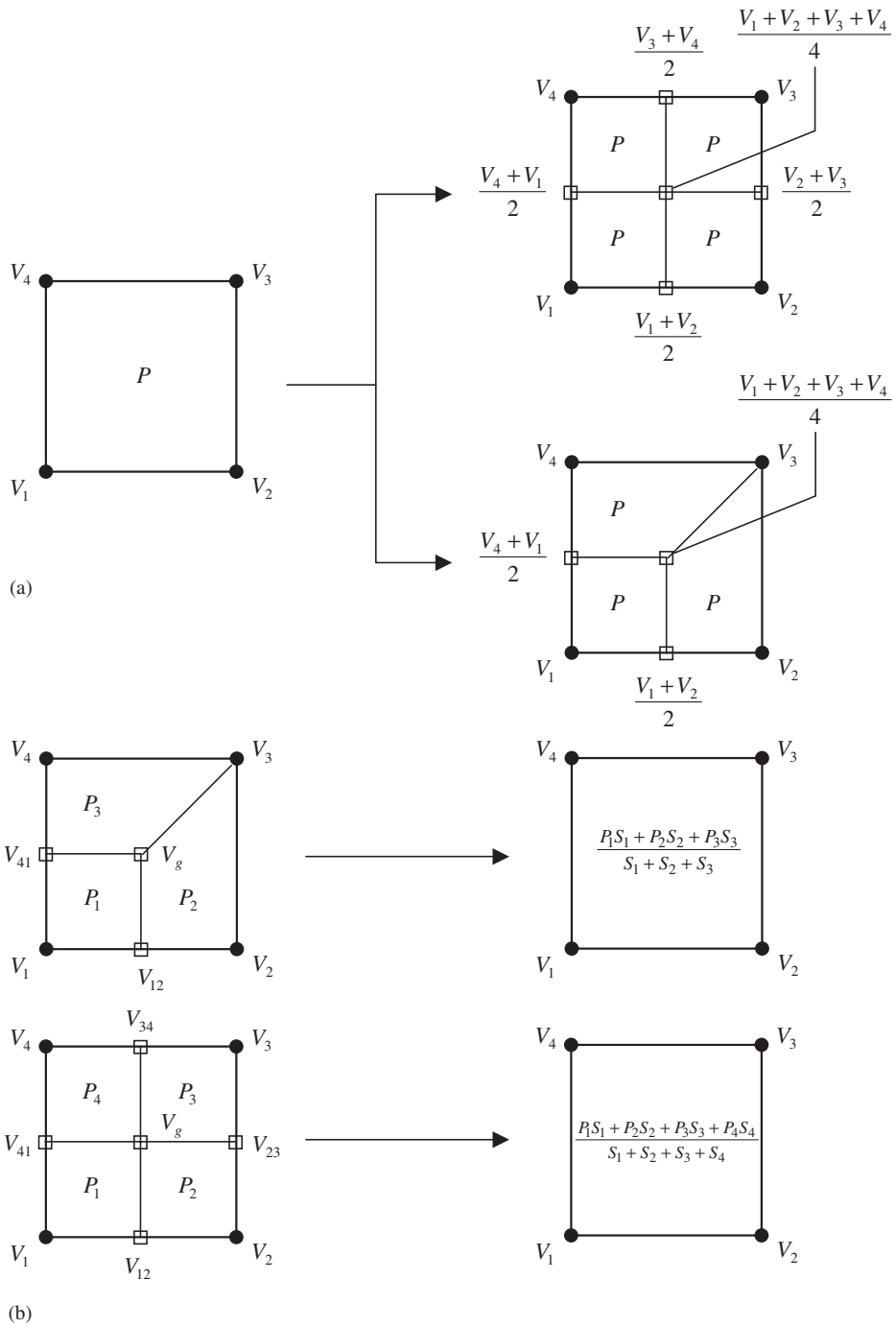


Figure 8. Interpolations of the values defined at nodes and elements: (a) interpolations in the grid fining and connection (b) interpolations in the grid coarsening.

 

The grids in the smoothing band are divided to the maximum division level according to the above procedure at the beginning of calculation. Then, this algorithm is adopted every time steps in which the adaptive mesh refinement is carried out.

## 5. RESULTS AND DISCUSSION

### *5.1. Collapse of a water column*

In order to prove the validity of the numerical scheme, collapse of a water column is computed first by the conventional level set method and the level set method coupled with the adaptive mesh refinement, which are, respectively, called LSM and LSM-AMR hereafter. The present results are compared with the numerical results and the experimental data obtained by Koshizuka *et al.* [35]. The calculation domain is shown in Figure 9. The size of a rectangular water tank is 58.40 cm in length and 40.88 cm in height. A water column is initially put on the left side with a rectangular shape, which is 14.60 cm in length and 29.20 cm in height. The top of the water tank is closed, and the slip condition is imposed on all walls. In the governing equation (2), the Reynolds number is fixed at 72 139, and the Bond number is set at infinity on the ground that the effect of surface tension is very small due to large representative length. The increment of time is 0.005, and the adaptive mesh refinement is done every five steps, i.e. $\Delta t' = 0.025$. Initially, the calculation domain is divided equally with the two-dimensional quadrangular grids in the following five ways: $10 \times 7$, $20 \times 14$, $40 \times 28$, $80 \times 56$ and $160 \times 112$. The smoothing bandwidth $\varepsilon$ is equal to the length of four grids in every case, and this standard is applied to all the calculations hereafter. The density and the coefficient of viscosity are 998.24 kg m$^{-3}$ and 0.85440 mPa s in water, 1.1763 kg m$^{-3}$ and 0.018621 mPa s in air, respectively.

Plate 1 shows the comparison of histories of the leading edge positions obtained from the numerical simulation and the experiment. Here, four grid sizes, which correspond to $20 \times 14$, $40 \times 28$, $80 \times 56$ and $160 \times 112$, are used for the calculation with LSM, and Koshizuka *et al.* adopted the moving particle semi-implicit (MPS) method for the simulation. As shown,

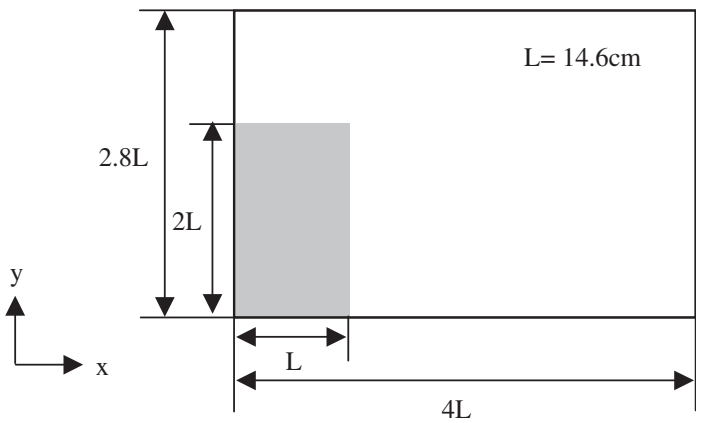


Figure 9. Schematic diagram of the calculation model for collapse of a water column.

 

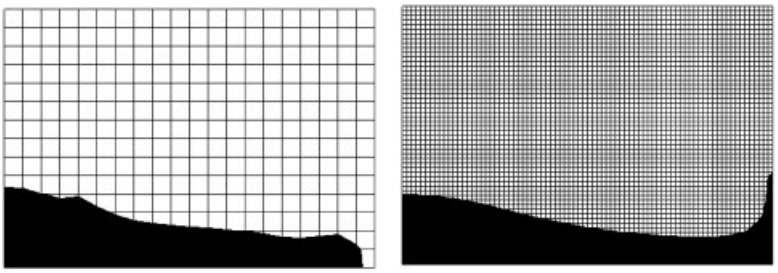

(a) Grid and water column: 0.3s
Cell: 280, Node: 315

(b) Grid and water column: 0.3s
Cell: 4480, Node: 4617

Figure 10. Comparison of transient shapes of a water column obtained with LSM in two different grid systems: (a) $20 \times 14$; (b) $80 \times 56$.

the present results are getting closer to the numerical result of Koshizuka *et al.* as the number of grids increases. This indicates the importance of grid resolution in LSM. The reason why the speed of the leading edge measured by the experiment is slower compared to the numerical results is that the wet condition between the leading edge and the bottom wall is not considered in the simulation. Since the histories in $80 \times 56$ and $160 \times 112$ grids are almost the same, the calculated results obtained with the former grid system are used hereafter as the standards of accuracy.

The transient shapes of a water column obtained with LSM in $20 \times 14$ and $80 \times 56$ grids are compared in Figure 10. As shown in Figure 10(a), the calculated result becomes rough due to the cumulative errors when the coarse grid system is used. On the contrary, the shape becomes fairly smooth in the fine grid system as shown in Figure 10(b) and corresponds well to the result obtained with the MPS method [35] qualitatively.

The transient shapes of a water column based on three different division levels in LSM-AMR are compared in Figure 11. Here, the maximum division level is set at 1 in $40 \times 28$ initial grids, 2 in $20 \times 14$ initial grids and 3 in $10 \times 7$ initial grids; the minimum element length becomes equal to an element length of the division $80 \times 56$ in every case and one-eighth of the initial length in the division level 3. As shown, the number of grids gets smaller as the maximum division level increases. In Figure 11(i), it is nearly equal to a quarter of $80 \times 56$. Nevertheless, the calculated results are almost the same at 0.1, 0.2 and 0.3 s; moreover, they are in good agreement with the results obtained with LSM in Figure 10(b) and the MPS method qualitatively. This is confirmed in the velocity distribution shown in Plate 2. Although the grids located away from the free surface are distributed coarsely in Plate 2(b), the velocity in the vicinity of the interface is calculated accurately with fine grids; accordingly the movement of the interface can be simulated correctly. In fact, the maximum velocities obtained with LSM in Plate 2(a) and LSM-AMR based on the division level 3 in Plate 2(b) are fairly close: 3.30 and 3.27 m $s^{-1}$, respectively.

Plates 3 and 4 show the comparison of histories of the leading edge positions and the global mass preservation obtained with LSM and LSM-AMR, which correspond to the results shown in Figures 10(b) and 11, respectively. In every case, good agreement with the numerical result of Koshizuka *et al.* is shown, and the mass is always preserved very well.

Comparison of computation time and total iteration number until 0.3 s obtained in the above analysis is listed in Table I. In this study, all computations are performed in a Pentium

 

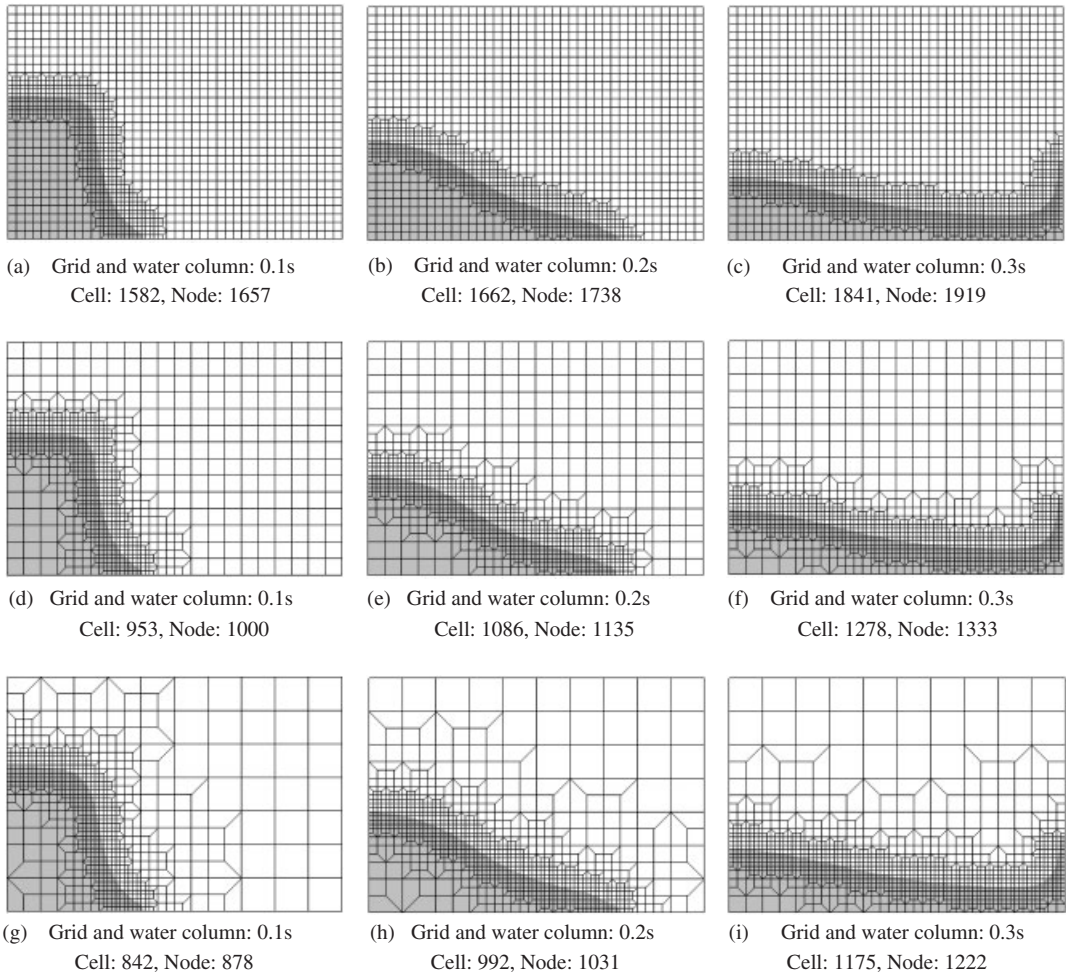

(a) Grid and water column: 0.1s
Cell: 1582, Node: 1657

(b) Grid and water column: 0.2s
Cell: 1662, Node: 1738

(c) Grid and water column: 0.3s
Cell: 1841, Node: 1919

(d) Grid and water column: 0.1s
Cell: 953, Node: 1000

(e) Grid and water column: 0.2s
Cell: 1086, Node: 1135

(f) Grid and water column: 0.3s
Cell: 1278, Node: 1333

(g) Grid and water column: 0.1s
Cell: 842, Node: 878

(h) Grid and water column: 0.2s
Cell: 992, Node: 1031

(i) Grid and water column: 0.3s
Cell: 1175, Node: 1222

Figure 11. Comparison of transient shapes of a water column based on three different maximum division levels in LSM-AMR: (a)–(c) level 1; (d)–(f) level 2; (g)–(i) level 3.

Table I. Comparison of computation time and total iteration number until 0.3 s.

| | LSM ($20 \times 14$) | LSM ($80 \times 56$) | LSM-AMR 1 | LSM-AMR 2 | LSM-AMR 3 |
|---|---|---|---|---|---|
| Time | 0 min 32 s | 26 min 30 s | 13 min 7 s | 7 min 58 s | 7 min 15 s |
| Iteration num. | 698 | 8288 | 11 718 | 18 860 | 25 903 |

III/600 MHz PC. According to the table, the computation time in LSM-AMR is about a half for the division level 1 and less than one-third for the division levels 2 and 3 of that in LSM with $80 \times 56$ grids. However, the iteration number, which is shown $m$ in Figure 1, becomes

 

larger as the maximum division level increases. This reflects the instability of calculation due to the difference in grid size. Although the maximum division level can be set freely, the error in the equation of continuity becomes large in case the difference in grid size is noticeable since the flow state is not taken into consideration in the present adaptive mesh refinement. Therefore, the maximum division level is fixed at 2, in which the minimum element length becomes one-fourth of the maximum element length, hereafter.

Through this analysis, the validity and effectiveness of LSM-AMR are proved. By applying it to the simulation of collapse of a water column, the computational efficiency is successfully improved. However, the frequency of the adaptive mesh refinement should be set carefully. The iterative calculation of the Poisson equation increases in number just after the mesh refinement since the interpolated velocity, which is given to the new nodes, does not satisfy the equation of continuity. For that reason, the computational efficiency slips if the time step $\Delta t'$ is set small. On the contrary, the discrepancy in position between fine grids and a calculated free surface may arise if it is set large. Therefore, the size of the time step should be determined by the trade-off between calculation speed and accuracy.

### *5.2. Oscillation of a drop under zero gravity*

In the preceding example, the effect of surface tension can be neglected as being small. However, if a liquid object is small and put under low gravity, the restoring force becomes dominant due to reduction in the Weber number in Equation (3). In order to prove the effectiveness of LSM-AMR again on such a condition, the oscillation of a drop is simulated in this section.

Figure 12 shows the calculation domain, which is inside a square container. A drop, whose initial shape is also a square, is floated in the centre of the domain under zero gravity, and its length of a side is set half of that of the container. First, in order to verify the numerical scheme, the oscillation of an ethanol drop is calculated with LSM on the same condition that Brackbill *et al.* [30] set in their numerical analysis. The density, coefficient of viscosity and surface tension in ethanol are $797.88\,\mathrm{kg\,m^{-3}}$, $1.1968\,\mathrm{mPa\,s}$ and $23.61\,\mathrm{mN\,m^{-1}}$, respectively, while the same physical properties as Section 5.1 are used for air. The length of a side of the container is 7.5 cm. Next, non-dimensional analysis is carried out in order to evaluate the usefulness of LSM-AMR. Here, the physical properties of water are used as representative values, and the ratios between gas and liquid in density and the coefficient of viscosity are

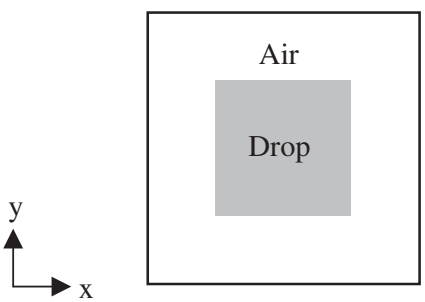


Figure 12. Schematic diagram of the calculation model for an oscillatory drop under zero gravity.

 

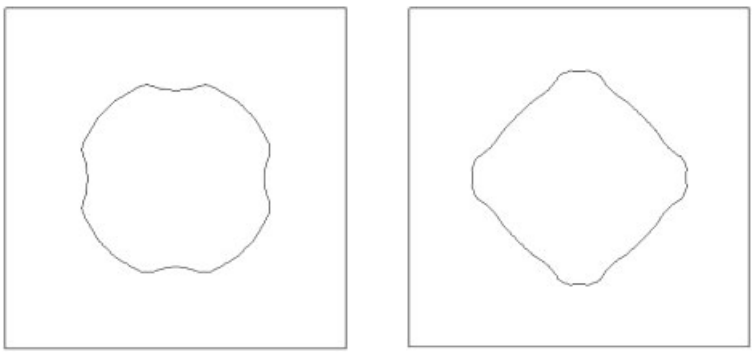


Figure 13. Transient shapes of an ethanol drop.

$\rho_G/\rho_L = 0.001$ and $\mu_G/\mu_L = 0.01$, respectively. The Reynolds number is fixed at 1000, while the following three values are chosen for the Weber number: 50, 200 and 800. The length of a side of the container is 2. In this analysis, the temperature field is not considered. Thus, the third term on the right-hand side in Equation (3) is omitted. As a boundary condition, the non-slip condition is imposed on all walls. The increments of time are, respectively, 0.1ms and 0.01, and the adaptive mesh refinement is done every 20 steps, i.e. $\Delta t' = 0.2$. The calculation domain is divided equally with $20 \times 20$ or $80 \times 80$ grids; the adaptive mesh refinement is applied to the former grid system, and the ethanol drop oscillation is calculated with the later.

The transient shapes of an ethanol drop at 0.1 and 0.2 s are shown in Figure 13. Since the drop is initially square in shape, large inward restoring force is produced at each apex immediately after the calculation starts. Then, the drop is deformed gradually to reduce the curvature there; accordingly the sides of a square drop are curved to preserve the volume. Afterward, the same is repeated again and again; parts of the drop surface with large curvature are dented by large restoring force, whereas the other parts are swelled up. However, as the time passes, this oscillation in shape declines due to viscosity and numerical dissipation, and finally the drop becomes stationary with a round shape. The present results are qualitatively in good agreement with those obtained by Brackbill *et al.* [30] with the VOF method.

Plate 5 shows the transient shapes of a water drop, distribution of velocity and the surface force, which corresponds to the fourth term on the right-hand side in Equation (3), at $t = 2$, 4 and 6 on the case of $We = 200$; Plates 5(a)–5(c) and 5(d)–5(f) are obtained with LSM in $20 \times 20$ and $80 \times 80$ grids, respectively, and Plates 5(g)–5(i) are done with LSM-AMR. If coarse grids are used in LSM, the shape of a drop becomes rough as shown in Plates 5(a)–5(c) due to poor distribution of velocity and surface force. In contrast, the shape of a drop becomes smooth as shown in Plates 5(d)–5(f) when fine grids are provided. Here, the surface force is well concentrated in the vicinity of the free surface. The calculated results shown in Plates 5(g)–5(i) agree reasonably well with those in Plates 5(d)–5(f) with regard to shape and distribution of the surface force; besides, they are quantitatively close in the maximum velocity at any time. This is due to the fact that the restoring force, which is produced only in the smoothing band, is calculated accurately at all times with fine grids according to the present rule for grid fining.

 

Table II. Comparison of computation time until $t = 200$ at $We = 200$.

| | LSM ($20 \times 20$) | LSM ($80 \times 80$) | LSM-AMR |
|---|---|---|---|
| Time | 11 min 32 s | 262 min 9 s | 129 min 4 s |

Table III. Comparison of computation time until $t = 200$ at $We = 50$ and 800.

| $We$ | LSM ($80 \times 80$) | LSM-AMR |
|---|---|---|
| 50 | 329 min 13 s | 161 min 38 s |
| 800 | 238 min 11 s | 101 min 48 s |

Plate 6 shows the comparison of histories of drop oscillation obtained with LSM in two different grid systems and LSM-AMR. Here, the radius of a drop, which is equal to 0.5 at the initial state, is plotted on the graph. As shown, the period of oscillation becomes longer in LSM with $20 \times 20$ grids than that in LSM with $80 \times 80$ grids. This is caused by the fact that the restoring force, which depends on curvature, is calculated smaller in the coarse grid system. However, the calculated results based on LSM with $80 \times 80$ grids and LSM-AMR are quantitatively in good agreement and correspond to the exact value at the steady state. It should be emphasized that the number of grids and the computation time in LSM-AMR are, respectively, about one-third and a half of those in LSM as shown in Plates 5(g)–5(i) and Table II.

In order to prove the effectiveness of LSM-AMR in a wide range of surface tension, calculation is conducted further with two different Weber numbers, i.e. $We = 50$ and 800. Plates 7 and 8 show the comparison of histories of drop oscillation obtained with LSM in $80 \times 80$ grids and LSM-AMR at $We = 50$ and 800, respectively. As shown, the period of oscillation becomes shorter in small Weber number due to the strong restoring force. In both graphs, good agreement can be seen between the calculated results. However, by contrast, the computation time in LSM-AMR is less than a half of that in LSM in both cases as shown in Table III.

### *5.3. Movement of a drop under zero gravity*

In this section, the movement of a drop due to the Marangoni effect is analysed by introducing the temperature field. Since the Marangoni effect works on the tangential plane to a free surface as shown in the third term on the right-hand side in Equation (3), its contribution to deformation is much less than that of the restoring force shown in the fourth term. However, a drop can be moved in some direction by the shearing force produced on the free surface. The purpose of this analysis is to prove the effectiveness of LSM-AMR in the simulation of such a phenomenon.

First of all, the validity of the numerical scheme is checked with the calculation model shown in Plate 9. A rectangular container is filled with two kinds of liquids, which do not mix together, under zero gravity. The container is 60 mm in length and 40 mm in height, and the interface is formed at a height of 20 mm from the bottom. The temperatures on

 

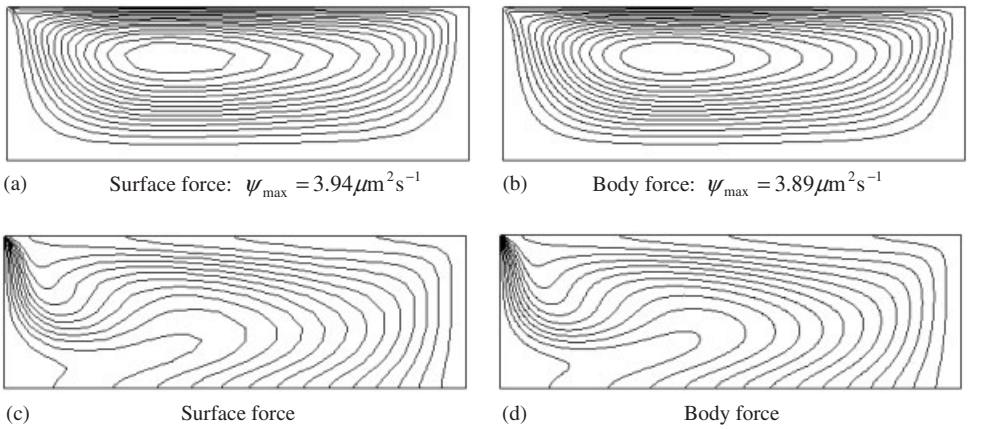


Figure 14. Comparison of the flow configurations: (a), (b) streamlines ($\Delta\psi = [\psi_{max} - \psi_{min}]/15$); (c), (d) isotherms ($\Delta T = [T_{max} - T_{min}]/15$) at 30 s.

the right and left walls are fixed at 363.15 and 283.15 K, respectively, while the adiabatic condition is imposed on the other walls. As a boundary condition in the velocity field, the non-slip condition is imposed on all walls. At the initial state, the liquids are at rest with the linear profile in temperature from the hot wall to the cold wall. Both of the liquids are the same in density and viscosity, which are 915 kg m$^{-3}$ and 45.75 mPa s, respectively. As a result, the flow field becomes symmetrical with respect to the interface. The thermal coefficient of surface tension is $-0.068$ mN m$^{-1}$ K$^{-1}$. The Marangoni effect induced by the gradient of surface tension is calculated both as a surface force and a body force, which are, respectively, shown in Plates 9(a) and 9(b). In the former, the jump quantity on the free surface is introduced into the boundary term as follows [36]:

$$\rho \bar{M}_{\alpha\beta} \frac{\tilde{\mathbf{v}}_\beta - \mathbf{v}_\beta^n}{\Delta t} = -\rho(\mathbf{v}_e^n \cdot \mathbf{A}_{\alpha\beta})\mathbf{v}_\beta^n - \frac{\rho\Delta t}{2} B_{\alpha\beta}\mathbf{v}_\beta^n + \mathbf{C}_\alpha p_e^n - \mu D_{\alpha\beta}\mathbf{v}_\beta^n + \mathbf{S}_\alpha$$

$$\mathbf{S}_\alpha = \int_{\Gamma_2^e} N_\alpha \{\mathbf{t}^{(n)}\}_e^n \, d\Gamma = \int_{\Gamma_2^e} N_\alpha \{\sigma_T \nabla_{//} T - \sigma_S(\nabla \cdot \mathbf{n})\mathbf{n}\}_e^n \, d\Gamma \tag{11}$$

while the latter is calculated according to Figure 1. In both cases, the restoring force can be neglected due to the flatness. The increment of time is 1 ms, and the computation continues until 30 s, at which the fluid flow is in the steady state. The number of grids is $60 \times 20$ in Plate 9(a) and $300 \times 100$ in Plate 9(b); the grids are concentrated near the boundaries in the former, while they are divided equally in the latter.

Figure 14 shows the comparison of the steady flow configurations with streamlines and isotherms. As shown, the calculated results based on the two different methods are qualitatively in good agreement with each other in the flow field and the temperature field. Moreover, they are close in the maximum value of the stream function.

The validity of the present scheme is also proved quantitatively in Plate 10. This graph shows the comparison of velocity on the centreline of the container obtained with two

 

numerical methods and theory, which is described in the following equation:

$$v_x = \frac{\sigma_T(\partial T/\partial x)}{4H\mu_L}(3y^2 - Hy) \tag{12}$$

where $H$ is the height of a container. By substituting the temperature gradient $\partial T/\partial x = 346\,\mathrm{K\,m^{-1}}$ and other parameters into Equation (12), it is rewritten as $v_x = -3.21(3y^2 - 0.04y)$. As shown, again, the agreement is reasonably good.

Next, the movement of a drop due to the Marangoni effect is solved by LSM and LSM-AMR. Plate 11 shows the calculation model. A water drop is floated and moved on the centreline of a square container under zero gravity. The length of a side of the container $(L, H)$ is 4, and initially a drop, whose radius is 0.5, is located at a height $(H_i)$ of 1 from the bottom. Since the axisymmetry is assumed, the calculation domain corresponds to half of the container. The initial temperature on the bottom wall is set at 1, while that on the top wall is zero; the temperature on the side wall is distributed linearly from zero to 1, which corresponds to the initial temperature of fluid. The physical properties of water are used as representative values, and the ratios between gas and liquid in density, and thermal diffusivity are $\rho_G/\rho_L = 0.001$, $\mu_G/\mu_L = 0.01$ and $\alpha_G/\alpha_L = 150$, respectively. The Reynolds number, Peclet number, Weber number and Marangoni number are, respectively, 1000, 7000, 200 and $-10\,000$. The temperature on the side wall is unchangeable, whereas the adiabatic condition is imposed on the top and bottom walls. In the velocity field, the non-slip condition is imposed on the side wall, while the slip condition is done on the top and bottom walls. The increment of time is 0.01, and the adaptive mesh refinement is done every 25 steps, i.e. $\Delta t' = 0.25$. The calculation domain is divided equally with $25 \times 50$ or $100 \times 200$ grids, and the adaptive mesh refinement is applied to the former grid system.

In the condition of this analysis, a water drop rises gradually due to the gradient of surface tension on the free surface, i.e. Marangoni effect since the temperature in the lower part of the drop is higher than that in the upper part. The drop is kept with a round shape because the distortion due to the shearing force is suppressed by the restoring force. Figure 15 shows the comparison of transient positions of a drop and isotherms at $t = 20$, 60 and 100; Figures 15(a), 15(c) and 15(f) are obtained with LSM, and Figures 15(b), 15(d) and 15(f) are done with LSM-AMR. As shown, the calculated results are strikingly similar in the position of a drop and temperature distribution; besides they are quantitatively close in the maximum velocity. This is due to the fact that the shearing force, which is produced only in the smoothing band, as well as the restoring force is calculated accurately at all times with fine grids in LSM-AMR. The sentence above is confirmed in the velocity distribution shown in Plate 12.

Plate 13 shows the comparison of histories of the drop head position obtained with LSM in two different grid systems and LSM-AMR. As shown, the calculated results based on LSM with $100 \times 200$ grids and LSM-AMR are in good agreement although the result based on LSM with $25 \times 50$ grids is deviated from the two. One of the reasons why the speed of a rising drop becomes slightly higher in LSM-AMR is the error in terms of linear interpolation of temperature in the adaptive mesh refinement. The computation time in LSM-AMR is less than one-sixth of that in LSM with $100 \times 200$ grids according to Table IV; the smallest rate is achieved. This reflects the difference in number of grids as shown in Figure 15; the number in LSM-AMR is almost one-tenth of that in LSM at any time. Thus, it can be said that LSM-AMR is effective, especially in the case that a relatively small object moves in a large calculation domain.

 

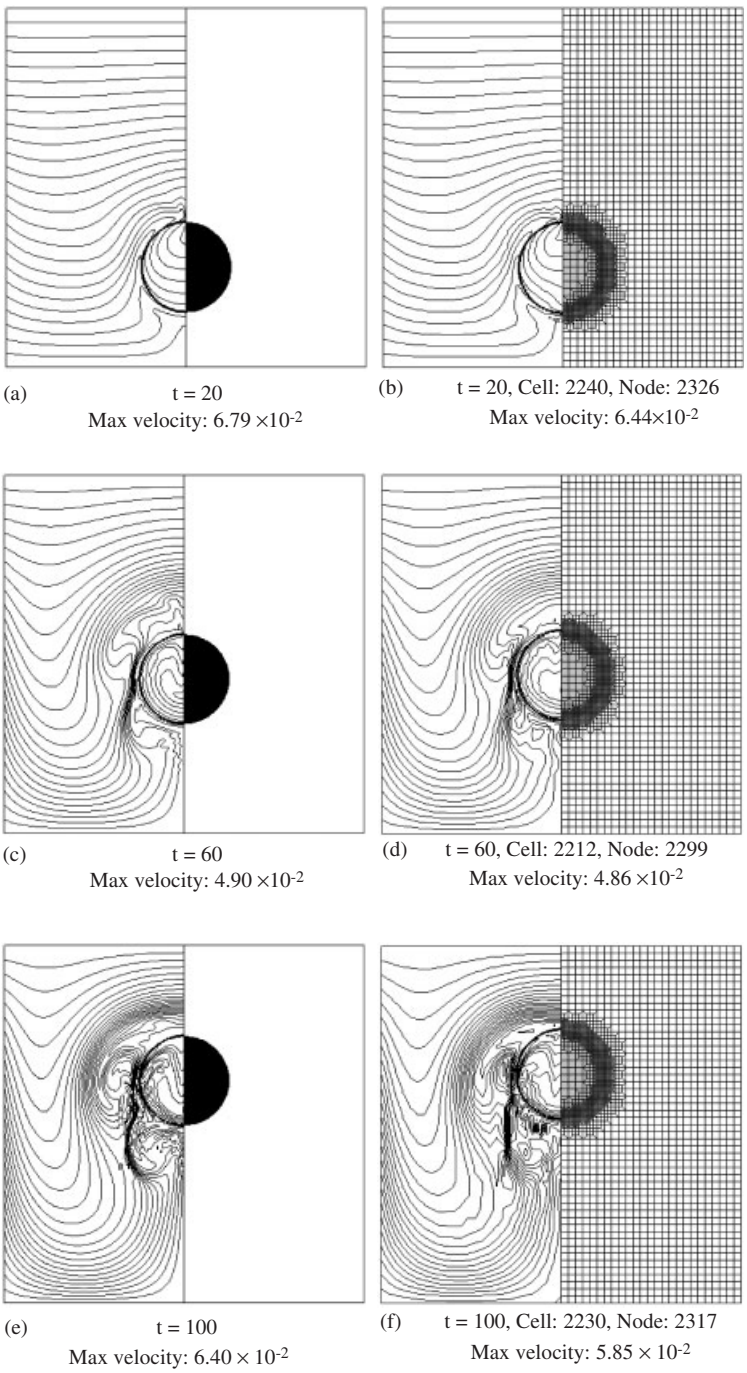


Figure 15. Comparison of transient positions of a drop and isotherms ($\Delta T = 0.04$): (a), (c), (e) LSM ($100 \times 200$); (b), (d), (f) LSM-AMR.

 

Table IV. Comparison of computation time until $t = 100$.

| | LSM ($100 \times 200$) | LSM-AMR |
|---|---|---|
| Time | 662 min 32 s | 97 min 23 s |

## 6. CONCLUSIONS

A numerical scheme has developed by coupling the level set method with the adaptive mesh refinement (LSM-AMR) in order to calculate a largely deformed free-surface problem accurately, economically and stably. The governing equations are discretized by FEM with the GSMAC scheme, and the reinitialization equation is solved by CIP-FEM. In the adaptive mesh refinement, the connective grids are used to exclude the intermediate nodes, so that it is easily introduced to the EFM-based algorithm. Here, the level set function is selected for the indicator, and the smoothing bandwidth is done for the threshold. In order to verify the validity of the proposed scheme, the collapse of a water column, the oscillation and movement of a drop under zero gravity were analysed and its performance was demonstrated. The calculation results show good agreement with other numerical results. Moreover, it is revealed that the calculation time is largely saved in all the cases in comparison with the conventional level set method. In the collapse of a water column, good agreement with other numerical results is shown in three division levels. The mass conservation is preserved very well in every condition. The computation time becomes less than one-third for the division levels 2 and 3 of that in LSM. In the oscillation of a drop, the effectiveness of the present scheme is shown in a wide range of Weber numbers, from 50 to 800. In every condition, the computation time becomes less than a half of that in LSM. Finally, the present scheme is applied to the movement of a drop due to the Marangoni effect, and its usefulness is proved from the correspondence of the transient temperature distribution and the drop position. The computation time becomes less than one-sixth of that in LSM.

ACKNOWLEDGEMENTS

The authors are grateful for the support from the Ministry of Education, Culture, Sports, Science and Technology of Japan under Grant-in-Aid for Scientific Research and Grant-in-Aid for JSPS Fellows.

REFERENCES

1. Cröll A, Kaiser Th, Schweizer M, Danilewsky AN, Lauer S, Tegetmeier A, Benz KW. Floating-zone and floating-solution-zone growth of GaSb under microgravity. *Journal of Crystal Growth* 1998; **191**:365–376.
2. Davidson PA. *An Introduction to Magnetohydrodynamics* (1st edn). Cambridge University Press: Cambridge, 2001; 387–404.
3. Floryan JM, Rasmussen H. Numerical methods for viscous flows with moving boundaries. *Applied Mechanics Reviews* 1989; **42**:323–341.
4. Harlow FH, Welch JE. Numerical calculation of time-dependent viscous incompressible flow of fluid with free surface. *Physics of Fluids* 1965; **8**:2182–2189.
5. Hirt CW, Nichols BD. Volume of fluid (VOF) method for the dynamics of free boundaries. *Journal of Computational Physics* 1981; **39**:201–225.

 

6. Nichols BD, Hirt CW, Hotchkiss RS. SOLA-VOF: a solution algorithm for transient fluid flow with multiple free boundaries. *Los Alamos Scientific Laboratory Report*, LA-8355, 1980.
7. Jeong JH, Yang DY. Finite element analysis of transient fluid flow with free surface using VOF (Volume-of-Fluid) method and adaptive grid. *International Journal for Numerical Methods in Fluids* 1998; **26**:1127–1154.
8. Kim MS, Lee WI. A new VOF-based numerical scheme for the simulation of fluid flow with free surface. Part I: new free surface-tracking algorithm and its verification. *International Journal for Numerical Methods in Fluids* 2003; **42**:765–790.
9. Osher S, Sethian JA. Fronts propagating with curvature-dependent speed: algorithms based on Hamilton–Jacobi formulations. *Journal of Computational Physics* 1988; **79**:12–49.
10. Sussman M, Smereka P, Osher S. A level set approach for computing solutions to incompressible two-phase flow. *Journal of Computational Physics* 1994; **114**:146–159.
11. Chang YC, Hou TY, Merriman B, Osher S. A level set formulation of Eulerian interface capturing methods for incompressible fluid flows. *Journal of Computational Physics* 1996; **124**:449–464.
12. Himeno T, Watanabe T, Konno A. Numerical analysis for propellant management in liquid rocket tank. *AIAA* 2001; **01**:3822.
13. Iafrati A, Mascio AD, Campana EF. A level set technique applied to unsteady free surface flows. *International Journal for Numerical Methods in Fluids* 2001; **35**:281–297.
14. Tezduyar T, Aliabadi S, Behr M. Enhanced-discretization interface-capturing technique (EDICT) for computation of unsteady flows with interfaces. *Computer Methods in Applied Mechanics and Engineering* 1998; **155**: 235–248.
15. Sochnikov V, Efrima S. Level set calculations of the evolution of boundaries on a dynamically adaptive grid. *International Journal for Numerical Methods in Engineering* 2003; **56**:1913–1929.
16. Hirt CW, Amsden AA, Cook JL. An arbitrary Lagrangian–Eulerian computing method for all speeds. *Journal of Computational Physics* 1974; **14**:227–253.
17. Ramaswamy B, Kawahara M. Arbitrary Lagrangian–Eulerian finite element method for unsteady, convective, incompressible viscous free surface fluid flow. *International Journal for Numerical Methods in Fluids* 1987; **7**:1053–1075.
18. Jung CH, Minowa T, Tanahashi T. Numerical analysis of molten metal under magnetic field using ALE method. *JSME International Journal Series A* 2002; **45**:153–160.
19. Metzger J, Schwabe D. Coupled buoyant and thermocapillary convection. *PhysicoChemical Hydrodynamics* 1988; **10**:263–282.
20. Lan CW, Kou S. Heat transfer, fluid flow and interface shapes in floating-zone crystal growth. *Journal of Crystal Growth* 1991; **108**:351–366.
21. Frank S, Schwabe D. Temporal and spatial elements of thermocapillary convection in floating zones. *Experiments in Fluids* 1997; **23**:234–251.
22. Zeng Z, Mizuseki H, Higashino K, Kawazoe Y. Direct numerical simulation of oscillatory Marangoni convection in cylindrical liquid bridges. *Journal of Crystal Growth* 1999; **204**:395–404.
23. Sumiji M, Nakamura S, Azami T, Hibiya T. Optical observation of solid-melt interface fluctuation due to Marangoni flow in a silicon liquid bridge. *Journal of Crystal Growth* 2001; **223**:503–511.
24. Imaishi N, Yasuhiro S, Akiyama Y, Yoda S. Numerical simulation of oscillatory Marangoni flow in half-zone liquid bridge of low Prandtl number. *Journal of Crystal Growth* 2001; **230**:164–171.
25. Tanahashi T, Okanaga H, Saito T. GSMAC finite element method for unsteady incompressible Navier–Stokes equations at high Reynolds numbers. *International Journal for Numerical Methods in Fluids* 1990; **11**: 479–499.
26. Tanahashi T, Oki Y, Henjes K. An application of GSMAC-FEM to electrically conducting fluid flows driven by Lorentz force. *International Journal of Computational Fluid Dynamics* 1993; **1**:233–248.
27. Fujieda T, Tanahashi T. Finite element analysis of visco-elastic flow under high shear rate using the GSMAC-method. *International Journal of Computational Fluid Dynamics* 2000; **13**:203–210.
28. Fujieda T, Wada S, Tanahashi T. Unified solution algorithm for solids and fluids. *JSME International Journal Series B* 2001; **44**:179–187.
29. Yabe T, Wang PY. Unified numerical procedure for compressible and incompressible fluid. *Journal of the Physical Society of Japan* 1991; **60**:2105–2108.
30. Brackbill JU, Kothe DB, Zemach C. A continuum method for modeling surface tension. *Journal of Computational Physics* 1992; **100**:335–354.
31. Hirt CW, Nichols BD, Romero NC. SOLA: a numerical solution algorithm for transient fluid flow. *Los Alamos Scientific Laboratory Report*, LA-5852, 1975.
32. Makihara T, Kakuta Y, Tanahashi T. The GSMAC-CIP method. *Computational Fluid Dynamics Journal* 1999; **8**:19–25.
33. Makihara T, Shibata E, Tanahashi T. Application of the GSMAC-CIP method to incompressible Navier–Stokes equations at high Reynolds numbers. *International Journal of Computational Fluid Dynamics* 1999; **12**: 301–314.


 

34. Zienkiewicz OC, Taylor RL. *The Finite Element Method—Volume 3 Fluid Dynamics* (5th edn). Butterworth-Heinemann: London, 2000; 169–217.
35. Koshizuka S, Oka Y. Moving-particle semi-implicit method for fragmentation of incompressible fluid. *Nuclear Science and Engineering* 1996; **123**:421–434.
36. Kohno H, Tanahashi T. An application of GSMAC-FEM to coupled natural and Marangoni convection in a square cavity. *International Journal of Computational Fluid Dynamics*, submitted.

 

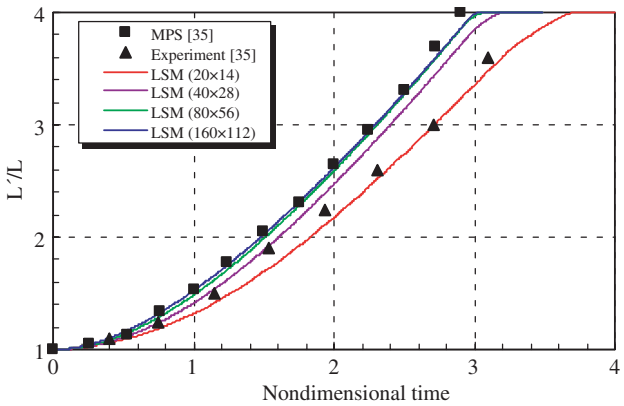


Plate 1. Comparison of histories of the leading edge position obtained with LSM in four different grid systems.

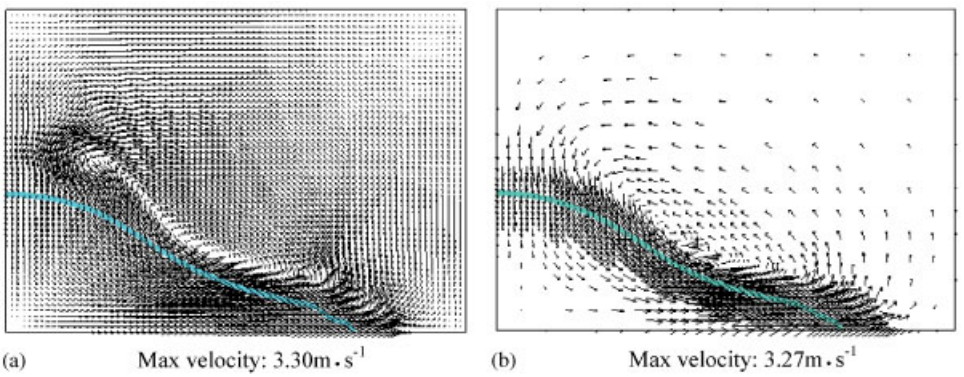


Plate 2. Comparison of velocity distributions and shapes of a water column at 0.2 s: (a) LSM ($80 \times 56$); (b) LSM-AMR (Level 3).

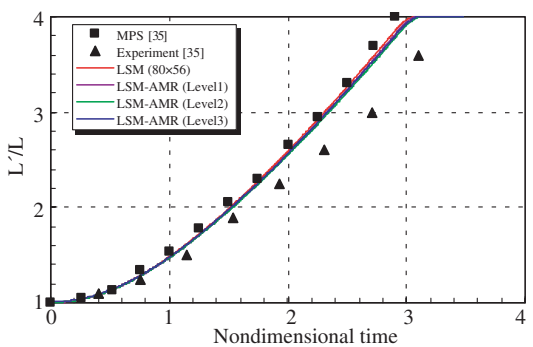


Plate 3. Comparison of histories of the leading edge position obtained with LSM and LSM-AMR.

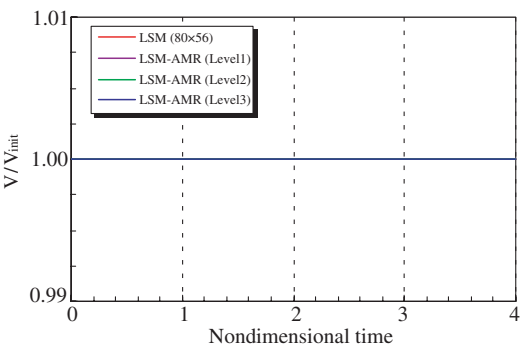


Plate 4. Comparison of histories of the mass preservation obtained with LSM and LSM-AMR.

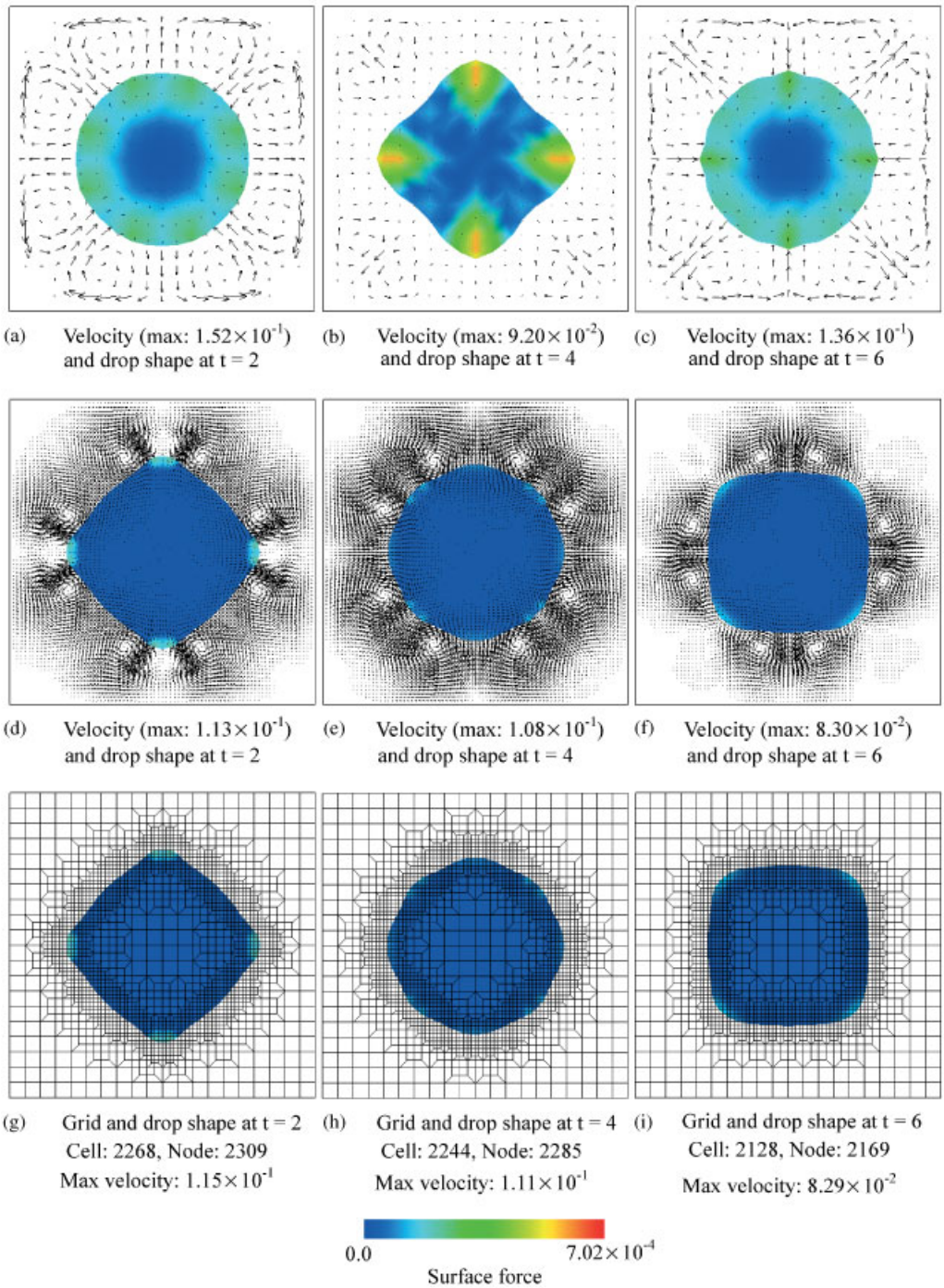


Plate 5. Comparison of transient shapes of a water drop and velocity distribution at $We = 200$: (a)–(c) LSM ($20 \times 20$); (d)–(f) LSM ($80 \times 80$); (g)–(i) LSM-AMR.

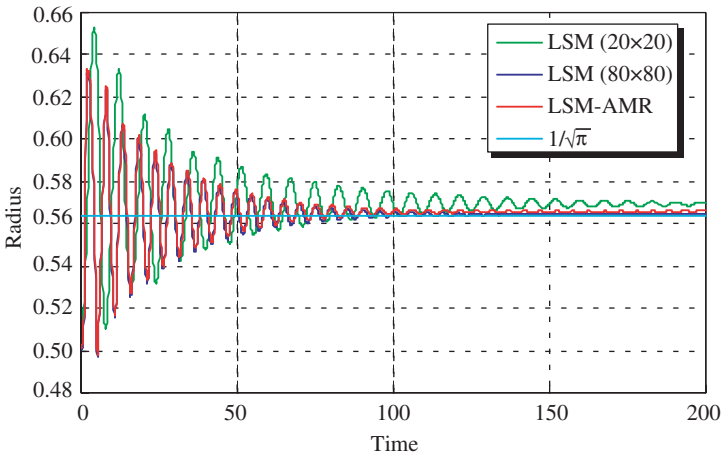


Plate 6. Comparison of histories of drop oscillation obtained with LSM and LSM-AMR at $We = 200$.

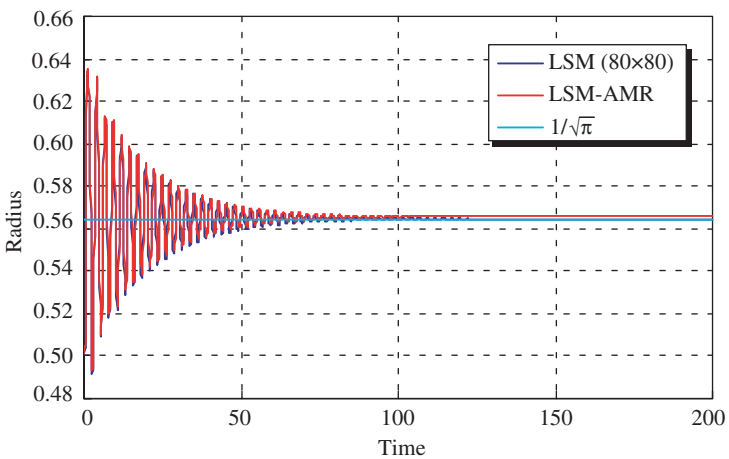


Plate 7. Comparison of histories of drop oscillation obtained with LSM and LSM-AMR at $We = 50$.

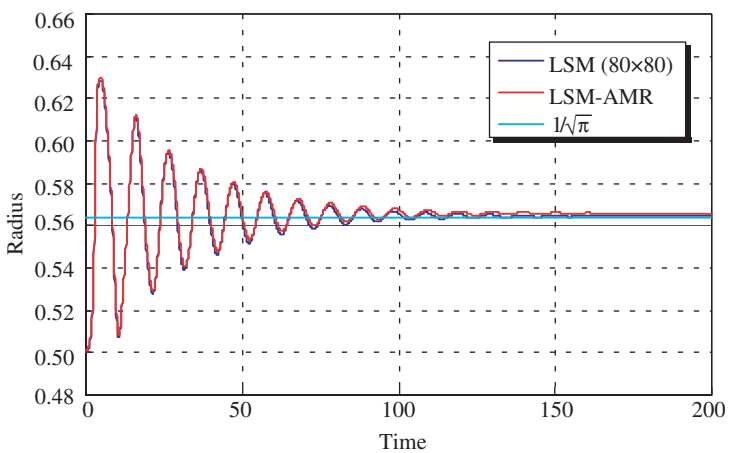


Plate 8. Comparison of histories of drop oscillation obtained with LSM and LSM-AMR at $We = 800$.

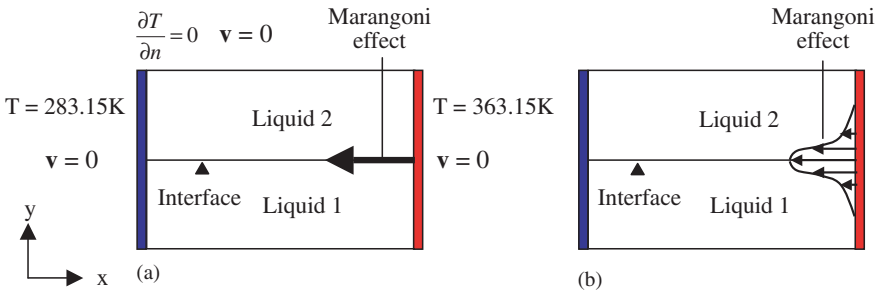


Plate 9. Schematic diagram of the calculation model used for verification of the Marangoni effect: (a) surface force and (b) body force.

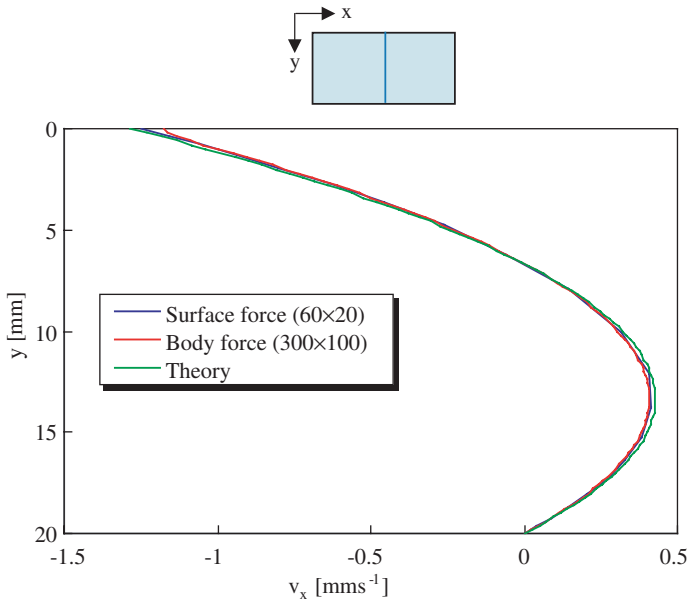


Plate 10. Comparison of velocity in the $x$ direction obtained with two numerical methods and theory at $x = 30$ mm, $t = 30$ s.

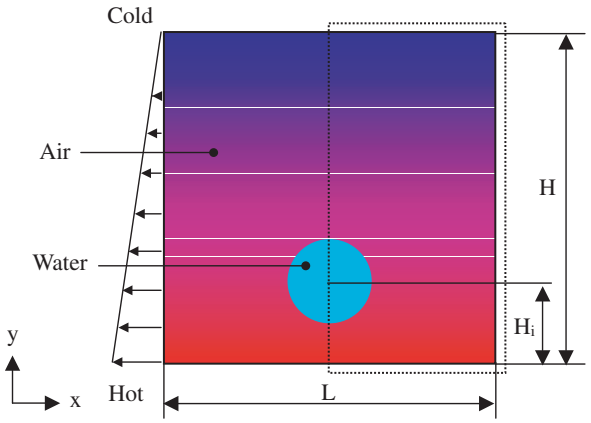


Plate 11. Schematic diagram of the calculation model for a rising water drop under zero gravity.

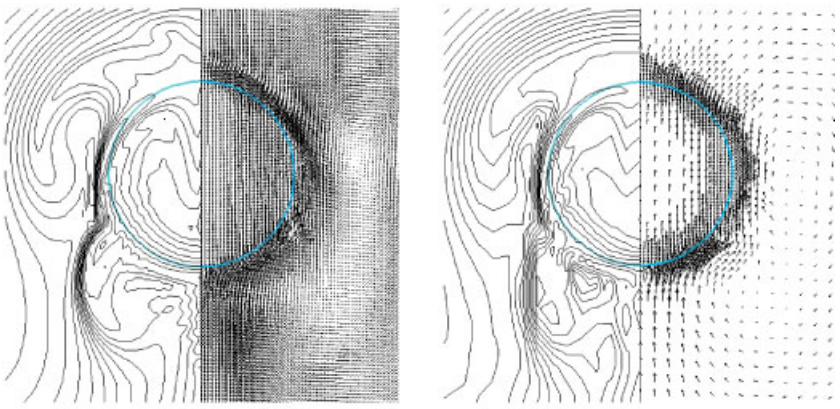


Plate 12. Comparison of isotherms ($\Delta T = 0.04$) and velocity distribution at $t = 80$: (a) LSM; (b) LSM-AMR.

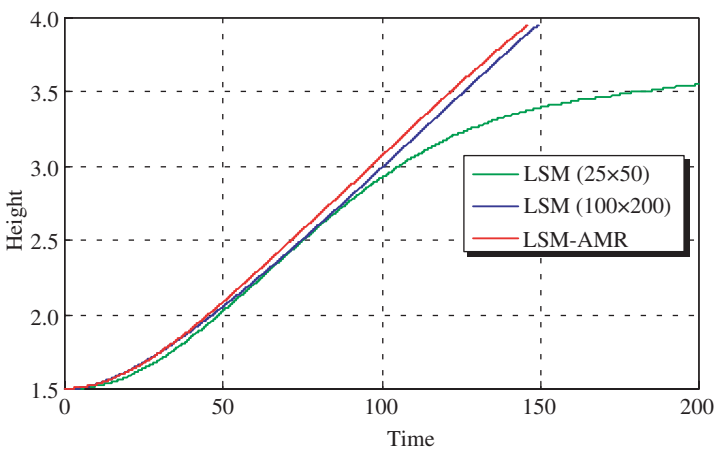


Plate 13. Comparison of histories of the drop head position obtained with LSM and LSM-AMR.